Synthesis and characterization of 2D-carbonylated graphitic carbon nitride: A promising organic semiconductor for miniaturized sensing devices

Thiago Martimiano do Prado [a,*], Lucas Gomes da Silva Catunda [a,b], Marcelo Luiz Calegaro [a], Daniel Souza Correa [b,*], Sérgio Antonio Spinola Machado [a,*]

[a] Institute of Chemistry of São Carlos, University of São Paulo, Avenida Trabalhador Sãocarlense, 400, São Carlos, SP 13560-970, Brazil
[b] Nanotechnology National Laboratory for Agriculture (LNNA), Embrapa Instrumentação, São Carlos, SP 13560-970, Brazil

ARTICLE INFO

ABSTRACT

Miniaturized chemical sensors are desirable for field analysis and screening trials aiming at point-of-care diagnostics. For this purpose, nanostructured materials, including those of the 2D family, are highly promising once they can add to sensing devices improved properties regarding sensitivity, the limit of detection, and portability. Here we report the synthesis, characterization, and application of 2D-carbonylated graphitic carbon nitride (c-g-C_3N_4) in the modification of screen-printed electrodes for photoelectrochemical analysis. Morphological and structural features of the material were studied through atomic force microscopy, scanning electronic microscopy, transmission electronic microscopy, X-ray diffraction, Fourier transformed-infrared spectrophotometry, and X-ray photoelectron spectroscopy. The optical bandgap of the semiconductor was estimated using diffuse reflectance spectrophotometry. Glucose determination was performed as proof of concept using c-g-C_3N_4 as support for the immobilization of glucose oxidase and application of the photoelectrochemical sensor. The device presented a linear range from 0 to 5.00 mmol L^{-1} and a limit of detection of 0.43 mmol L^{-1}. Our results indicate the suitability of employing c-g-C_3N_4 for designing photoelectrochemical sensors for detecting analytes of biological and medical interest.

1. Introduction

Recent advances in materials science and nanotechnology have allowed the development of smart materials possessing appealing optical [1], electrical [2], and mechanical properties [3] suitable for applications in medicine, energy, environmental science, and agriculture. Additional important features considered in the development of novel materials are their stability and low toxicity to enable large-scale production while mitigating environmental and health risks [4–6]. This premise is also valid for materials employed in electrochemical sensors modified with biological compounds (enzymes, antigens, antibodies, oligonucleotides, DNA, or RNA) [12–15], which ubiquitous use has been increasing in the last years for detecting analytes related to health, food and environmental safety [7–11,13]. Regarding electrochemical sensors, those operating under photoelectrochemical (PEC) mechanism have gained more attention recently, once they generally provide higher sensitivity [14–16]. Among the reasons, it can be mentioned that in PEC sensors the excitation source (light) and the detection signal (electrical)

have different nature and the baseline noise is generally low compared to other electrochemical sensors [16–18].

Graphitic carbon nitride (g-C_3N_4) is a non-toxic and biocompatible material relevant for energy conversion and storage applications [19–21], and more recently has also been proposed for photoelectrochemical (PEC) sensors [17,22–26]. This interesting organic semiconductor is usually used in combination with other materials aiming at the improvement of the charge transfer process [27–30]. However, the main challenge in the development of PEC sensors based on g-C_3N_4 is to obtain photocurrents that are inherent to the photoactivity of the pure material [31]. For the g-C_3N_4 synthesis, melamine, cyanamide, or urea [32] have been used as precursors, which are then subjected to thermal treatment, providing their polycondenzation and the formation of the graphite-like layered material. Since bulk g-C_3N_4 is obtained through this method, sonochemical top-down treatment should be performed for the fabrication of nanosheets [33], which approach is time-consuming and provides a low yield of exfoliated material.

---

* Corresponding authors.

E-mail addresses: thipra@gmail.com (T. Martimiano do Prado), daniel.correa@embrapa.br (D.S. Correa), sasmach@iqsc.usp.br (S.A.S. Machado).

In this work, a high-yield production method for 2D-carbonylated *g*-C$_3$N$_4$ nanosheets (*c-g*-C$_3$N$_4$) was developed, which were then applied to miniaturized sensors. Specifically, the exfoliation of bulk material was achieved using an ultrasound probe after acid treatment. Two-dimensional (2D) semiconductors materials offer the possibility of tuning the electronic properties through the manipulation of the dimensionality, strain, substrate engineering, and doping level [34]. Besides, the *c-g*-C$_3$N$_4$ low toxicity, easy preparation, and low cost are suitable for designing miniaturized and disposable PEC sensors with improved limit of detection and sensitivity [35]. In this context, here we developed a device using screen-printed electrodes (SPE) based on carbon ink and polyethylene terephthalate (PET) as substrate, which working electrode was modified with a thin layer of *c-g*-C$_3$N$_4$. The presence of the carbonyl groups on the semiconductor film favors the binding of structural terminations of enzymes, antibodies, and oligonucleotides. The device was tested in the presence of hexaammineruthenium (III) chloride used as a photoelectrochemical probe, with the enzyme glucose oxidase (GOx) immobilized over the *c-g*-C$_3$N$_4$ as a proof of concept.

2. Materials and methods

2.1. Chemicals

Melamine (99%), hexaammineruthenium (III) chloride (99.9% trace metals basis), glucose oxidase enzyme (GOx), sodium hydroxide, ammonium hydroxide (28%), sulfuric acid (98%), sodium phosphate monobasic ($\geq$ 99%), sodium, and sodium phosphate dibasic ($\geq$ 99%) were purchased from Sigma-Aldrich. Carbon ink was purchased from Loctite® (Eletrodag 423SS E&C). Polyethylene terephthalate substrate (PET), size 210 mm $\times$ 297 mm and thickness of 100 μm (Filipaper, Brazil) was obtained from a local market. All reagents were used without further purification, and aqueous solutions were prepared with ultrapure water (resistivity $\geq$ 18.2 MΩ.m).

2.2. Synthesis of c-g-C$_3$N$_4$

c-g-C$_3$N$_4$ was synthesized following the procedure available in the literature [36] with some modifications. Firstly, the *g*-C$_3$N$_4$ was produced by polycondenzation of the melamine under thermal treatment in a closed porcelain crucible in an oven at 550°C for 3 h, with a heating rate of 5°C min^{-1}. Next, the resultant yellow powder was used for preparing the carbonylated graphitic carbon nitride (*c-g*-C$_3$N$_4$) using acid treatment by addition of 0.5 g of *g*-C$_3$N$_4$ in 10 mL of H$_2$SO$_4$ (98%). The obtained colloidal suspension was maintained under stirring for 12 h at room temperature. Before the sonochemical treatment, the colloidal suspension was diluted in 50 mL of ultrapure water and, subsequently, was sonicated for 4 h at 20°C (at 60% of the maximum amplitude of the ultrasound probe) to promote exfoliation. Next, the suspension containing the exfoliated material was centrifuged at 10.000 rpm. The supernatant was discharged and the precipitate was washed again, with repetition of this step 5 times, until reaching pH 4.0. Finally, 50 mL of the suspension containing the *c-g*-C$_3$N$_4$ was stabilized by the addition of 5 μL of ammonium hydroxide (28%). The *c-g*-C$_3$N$_4$ concentration was determined by gravimetric analysis, which had an average value of 6 mg mL^{-1} (*n* = 3).

2.3. Screen-printed electrodes

Initially, the PET substrate was cleaned with isopropyl alcohol. Then, the carbon paste ink was spread onto the polyester screen (77-mesh) and manually transferred with the aid of a polyurethane squeegee to the PET sheet. Subsequently, the three printed electrodes were cured at 90 ºC for 30 min. Finally, the reference electrodes were painted with Ag/AgCl conductive ink and dried at 90ºC for 30 min. The geometric area of the working electrode was 12.56 mm^2.

2.4. Electrochemical pretreatment of SPE

The screen-printed electrodes (SPE) were submitted to an electrochemical pretreatment, to remove non-conductive substances from their surface. Thus, two cycles of cyclic voltammetry were performed in the presence of 0.5 mol L^{-1} H$_2$SO$_4$ at a potential range from –2.5 to +2.5 V and a scan rate of 100 mV s^{-1} [37].

2.5. Electrode modification

The working electrodes of pretreated SPE were modified by drop-casting 10 μL of the alkaline *c-g*-C$_3$N$_4$ suspension and dried out at room temperature overnight for the formation of a thin film.

2.6. GOx immobilization

Solutions with different GOx contents were prepared in 0.1 mol L^{-1} phosphate buffer saline, pH 7.0 before the immobilization over *c-g*-C$_3$N$_4$ (200 U mL^{-1}; 600 U mL^{-1}; 1400 U mL^{-1} and 2000 U mL^{-1}). Then, for each solution, an electrode was prepared by drop-casting 10 μL of the GOx solution, which resulted in 2, 6, 14, and 20 units per electrode, respectively. The electrodes were dried at room temperature. Next, 10 μL of 0.25% (v/v) glutaraldehyde solution was added over each electrode and kept for 20 min in a wet chamber. After, the electrodes were washed with ultrapure water and dried at room temperature.

2.7. Physical-chemical characterizations

The sonication of the *c-g*-C$_3$N$_4$ was performed with an ultrasound probe Vibra Cell^{TM} (Sonics) with the power of 130 W and a frequency of 20 kHz. All synthesized material was centrifuged using a Sorvall ST16 centrifuge (Thermo Scientific).

Electrochemical and photoelectrochemical experiments were carried out using a potentiostat/galvanostat Autolab 128 N (Metrohm). The data acquisition was done with NOVA 2.1.5 software. For the photoelectrochemical experiments, a UV LED with a power of 9 W was employed, which light source was coupled to a controller board (UNO) through a relay and operated via Arduino software.

X-ray diffractometry was performed by a D8 diffractometer (Brucker) with a Cu kα radiation source (λ = 1.54 Å). Fourier Transformed Infrared spectrophotometry (FT-IR) was done using a Tensor 27 spectrophotometer (Brucker). Transmission electron microscopy (TEM) was performed with an FEI Tecnai G^2 F20 HRTEM (ICN2). Scanning electronic microscopy (SEM) was performed with a JSM-6510 Series Scanning Electron Microscope (Jeol LTD.) and atomic force microscopy (AFM) was performed using Nanosurf Easyscan 2 (Nanosurf), operating in tapping mode with a Tap190Al-G tip (Budget Sensors).

X-ray photoelectron spectroscopy (XPS) experiments were carried out using an X-ray photoelectron spectrometer (Omicron-Scienta). Diffuse reflectance spectrophotometry (DRS) was carried out using a UV-2600 spectrophotometer (Shimadzu) equipped with an ISR-200 integration sphere.

3. Results

The yellow powder obtained after thermal treatment of melamine indicates the formation of *g*-C$_3$N$_4$ with a structure known as "melon" [38]. Thus, the melamine polycondenzation resulted in tris-s-heptazine A-B stacked structures [38]. Subsequent chemical attack with sulfuric acid leads to the formation of functional groups in terminations of the structure [32], while the sonochemical step provided the delamination of the functionalized structure [33]. The phenomenon results in cycles of molecules approaching and removal. However, the chemical reaction arises due to the effect of acoustic cavitation that warms up the liquid near 5000 $^{\circ}$C and generates pressure around 1000 atm in localized bubbles with a lifetime of milliseconds [34]. When the bubbles reach a
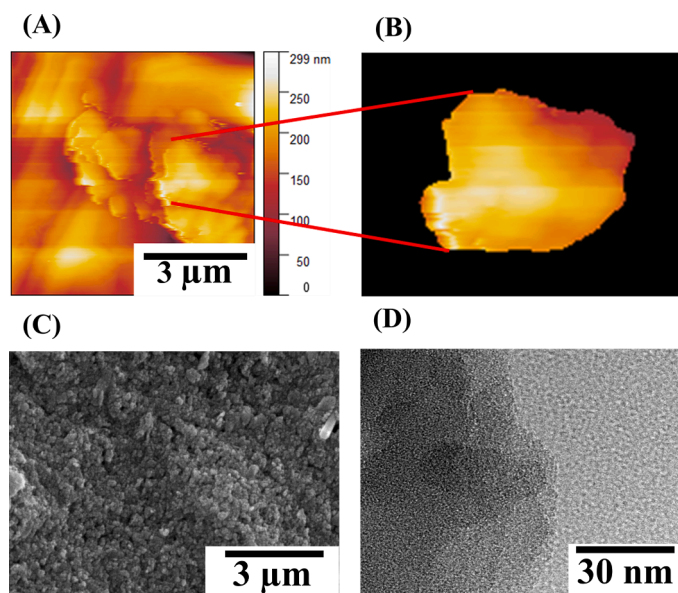
(A) **(B)**

(C) **(D)**

Fig. 1. (A) Images obtained by AFM for the c-g-C₃N₄ deposited onto the SPE, (B) Representative sheet for estimative area measurement, (C) SEM image of the c-g-C₃N₄ film and (D) TEM image of c-g-C₃N₄ sheet.

critical size of 170 μm, at the frequency of 20 kHz, they are collapsed causing the disruption of some chemical bonds in the g-C_3N_4. The hot spot theory explains the chemical reactions provided by the sonochemical treatment of the solution. In the c-g-C_3N_4 synthesis this application results in structural defects complementary to the acid step. Furthermore, the delamination and reduction of sheet size from c-g-C_3N_4 occurred in the sonochemical step.

Some exfoliation methods for g-C_3N_4 by sonochemical treatment can be found in the literature [35–39]. Nevertheless, most of them rely on ultrasound baths, which yield low efficiency for solution heating, thus requiring long times of exposition. Thus, the main advantage of our proposed method is the use of an ultrasound probe in direct contact with the sample. The product of the c-g-C_3N_4 synthesis was fully characterized by distinct techniques as follows.

3.1. Morphological characterization of c-g-C₃N₄

The morphology of the film formed on the SPE surface was verified by different techniques. In the AFM image presented in Fig. 1A, it is possible to observe the coating of the surface by 2D sheets of c-g-C_3N_4. From this image, a representative c-g-C_3N_4 sheet is highlighted in Fig. 1B, which has an area of xx384 nm², calculated with the aid of the software Image J. These results evidence the material was successfully

deposited on the SPE in its exfoliated form with a nanometer size.

The c-g-C_3N_4 film over the SPE surface was also investigated by SEM. Fig. 1C shows the micrography of c-g-C_3N_4 where it is noticeable the existence of a homogeneous structure formed by agglomerates of particulate material. Moreover, the TEM image in Fig. 1D shows in detail the morphology of the film with particles overlapping at a 2D-sheet constitution. These results corroborate the occurrence of the polymeric structure breakdown of g-C_3N_4 bulk, caused by the sonochemical treatment. Besides, after drying the particles union formed sheets as can be seen in the AFM and TEM images.

3.2. Structural characterization of c-g-C₃N₄

The results obtained by XRD (Fig. 2A) confirm the occurrence of changes in the g-C_3N_4 structure (sample 1) after chemical and sonochemical treatments, which gave rise to c-g-C_3N_4 (sample 2). The black diffractogram corresponds to sample 1 obtained after the heat treatment of melamine, and it has characteristic diffraction patterns for the bulk material and refers to the stacking of polymerized tris-s-triazine structures (Fig. 1S, supplementary material) [33]. Therefore, there is a more intense peak with a maximum of 2θ at 27.47°, which can be attributed to the 002 planes with a spacing of 0.324 nm. This value refers to the interplanar distance of the graphitic material. The peak at 2θ 12.98° is assigned to plane 100 with an interplanar spacing of 0.681 nm.

The red diffractogram in Fig. 2A was obtained for sample 2 after solvent evaporation from colloidal suspension after the sonochemical step. It is noticed the presence of peaks closer to sample 1, but narrower, which indicates the increase of the crystallinity after exfoliation. The peak with maximum intensity at $2\theta = 6.19°$ can be attributed to lamellae separation from the material during the sonochemical step ($d = 1.42$ nm). This result suggests the re-stacking of the exfoliated material after drying. The interlayer spacing has a significant value, even after the alleged stacking, and can be attributed to the presence of functional groups further explored by XPS analysis.

Fig. 2B shows the spectra with typical vibration modes of materials based on graphitic carbon nitride [40]. The reduction of the signal associated with the polymeric network of heptazine in the region between 2335 and 2370 cm⁻¹, in the red spectra, is attributed to N≡C after the exfoliation of the material in the sonochemical stage, which led to the cleavage of some structural bonds [35]. Is also observed an accentuation in the signal corresponding to the vibrations of N-H and O-H when the spectrum of sample 2 (red) is compared with that of sample 1 (black), which suggests a substantial reduction in the particle size of the exfoliated material [35]. In the region between 1600 and 1750 cm⁻¹, the signal enhancement is attributed to C=O of sample 2, which indicates that even after re-stacking the dry material lamellae, carbonylated groups are present.

X-ray photoelectron spectroscopy (XPS) was used to determine the functional groups formed on the surface of carbon nitrides produced by
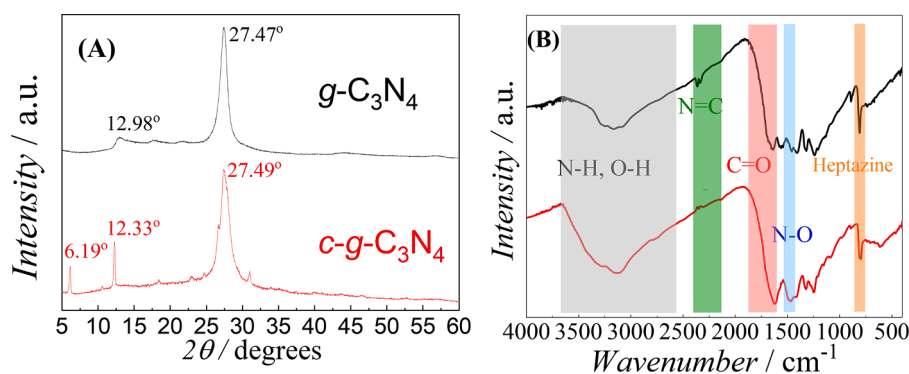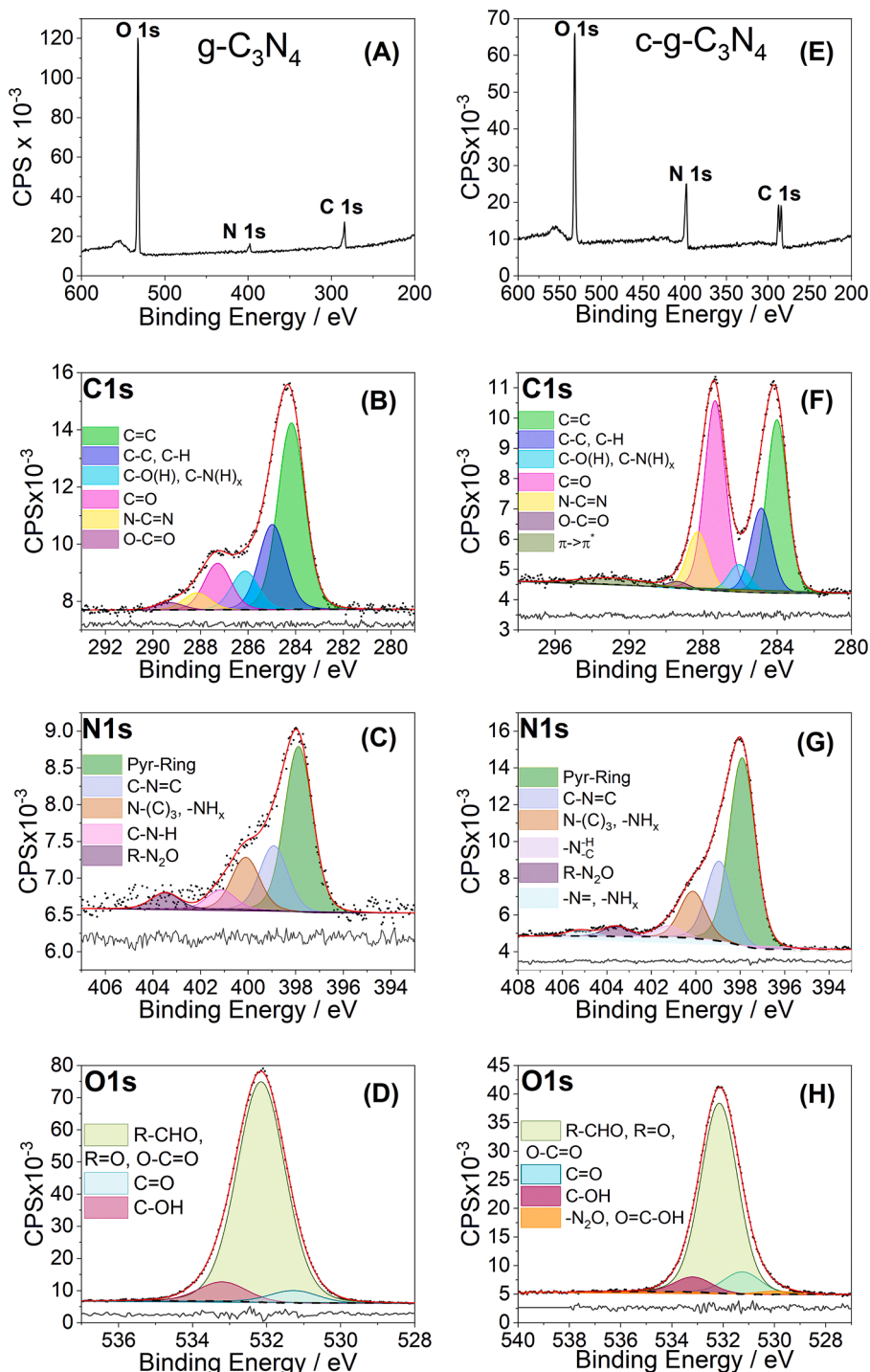
Fig. 2. (A) Diffractogram patterns of sample 1 (black) and sample 2 (red); (B) FT-IR spectra obtained for sample 1 (black) and sample 2 after drying the colloidal suspension (red).

Fig. 3. Sample 1: (A) survey, and high-resolution XPS spectra of (B) C 1 s, (C) N 1s, (D) O 1 s and sample 2: (E) survey, (F) C 1 s, (G) N 1s and (H) O 1 s.

thermal decomposition of melamine, bulk *g*-C$_3$N$_4$ (sample 1), and by subsequent acid treatment of sample 1 resulting in *c-g*-C$_3$N$_4$ (sample 2), as described into the experimental section. Fig. 3 presents high-resolution XPS spectra of C 1 s, N 1 s, and O 1 s for samples 1 and 2 respectively. The spectroscopic data obtained from the spectra presented in Fig. 3 are summarized in Tables 1S and 2S from supplementary material.. High-resolution C 1 s XPS spectra can be deconvoluted into six components for sample 1: (C=C) at 284.19 eV, (C-C, C-H) at 284.99, (C-O(H) or C-N(H)$_x$) at 286.14 eV, (C=O) at 287.28 eV, (N-C=N) at 288.16 eV and (O-C=O) at 289.29 eV. The sample 2 has the same contributions presented by sample 1 and an additional shake-up signal at 292.90 eV,

which are also known as shake-up satellites due to p→p* type transitions [46]. Sample 1 and sample 2 also presents a signal at 288.16 eV which can be assigned to sp^2-bonded carbons in the heptazine ring system (N-C=N) [47,48]. The survey spectra of both samples indicate a significant amount of oxygen incorporated as surface functional groups or as adsorbed water and carbon dioxide [2]. The high amount of oxygen detected in sample 1 is justified by the fact that the synthesis of this compound was conducted in an oxygenated atmosphere under elevated temperature, promoting the formation/adsorption of oxygen-containing species on the material surface. The deconvolution of sample 1 and sample 1 high-resolution XPS C 1s and O 1 s peaks indicates that the
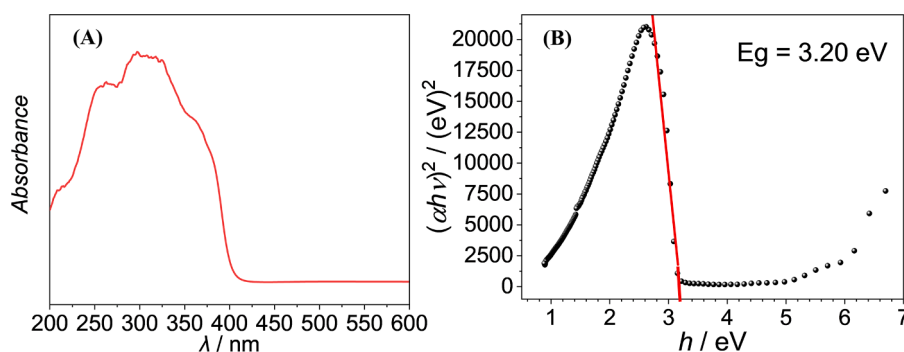
Fig. 4. (A) Absorbance spectrum of c-g-C$_3$N$_4$ in the UV-visible region. (B) Touc plot used to optical band gap determination by the intersection of the red line segment with the X-axis.

oxygenated functional groups on carbon nitride surfaces are composed of aliphatic alcohol, ketones, and carboxylic acid groups as well as aromatic aldehyde and quinone groups. Aromatic aldehydes and quinones are the main contributions to sample 1 O 1 s signal, suggesting that those species are produced by the oxidation of the aromatic heptazine ring system of melamine submitted to thermal treatment at high temperature in an oxygenated atmosphere. The diversification of functional groups formed on the carbon surface by this procedure may be considered a good strategy to form a more versatile substrate to produce chemical sensors and biosensors.

The acid chemical treatment to which sample 1 is submitted, generating sample 2, has an impact on the chemical surface composition of this compound, expressed mainly by the decrease of oxygen and increase of nitrogen and carbon contents. The decrease of oxygen signal may be related to the elimination of acid-soluble oxygen-containing species such as carbon dioxide and others. The acid treatment of sample 1 induces the increase of carbonylic groups as well as the diversification of nitrogenated surface groups; although the aromatic pyridyl group signal is the highest in both sample 1 and sample 2.

3.3. Diffuse reflectance spectrophotometry in the UV region

To be applied in photoelectroanalysis, it is essential to understand the energy bandgap (*Eg*) of *c-g*-C$_3$N$_4$ to define the radiation source necessary for proper device operation. Therefore, the diffuse reflectance spectrophotometry experiment was carried out in the UV-visible region. The absorption spectrum obtained is shown in Fig. 4A. The spectrum data were converted to percent reflectance using the Kubelka-Munk function. Then, the data were plotted on the Touc graph shown in

Fig. 4B and an *Eg* = 3.20 eV was obtained by the intersection of the red line segment with the *x*-axis. This value is higher than that of *g*-C$_3$N$_4$ reported in the literature (about 2.90 eV) [40] and typical for the decrease in particle size of the material [49]. Therefore, for a photocurrent to be produced by *c-g*-C$_3$N$_4$, the radiation incident on the surface must have energy greater than 3.20 eV. This was possible with the use of a 9 W power UV LED as a radiation source.

3.4. Photoelectrochemical behavior of c-g-C$_3$N$_4$

The behavior of the device for application in photoelectroanalysis was investigated in the presence of [Ru(NH$_3$)$_6$]Cl$_3$ in 0.1 mol L^{-1} phosphate buffer saline at pH 7.0. Under these conditions, it was possible to evaluate the existence of photocurrent for the material in an aqueous medium that could be used in the future for the analysis of samples containing biological material (plasma, saliva, urine, etc).

For the generation of a photocurrent with controlled potential is desirable that the response can be obtained in regions where capacitive current predominates, avoiding the interference of redox reactions caused by the applied potential. Thus, the observed photocurrent is due to the transfer of charges generated in the semiconductor to [Ru(NH$_3$)$_6$]Cl$_3$ acting as charge acceptor in solution. Fig. 5A shows the voltammogram obtained for SPE/*c-g*-C$_3$N$_4$ in 1 mmol L^{-1} [Ru(NH$_3$)$_6$]Cl$_3$ and 0.1 mol L^{-1} phosphate buffer saline at pH 7.0. The voltammogram shows that no Faradaic process occurs at 0 V potential. Therefore, the 0 V potential was considered ideal for performing chronoamperometry experiments with periodic irradiation of the device by the UV light source, which is called the on/off process.

The influence of [Ru(NH$_3$)$_6$]Cl$_3$ on the photocurrent intensity was
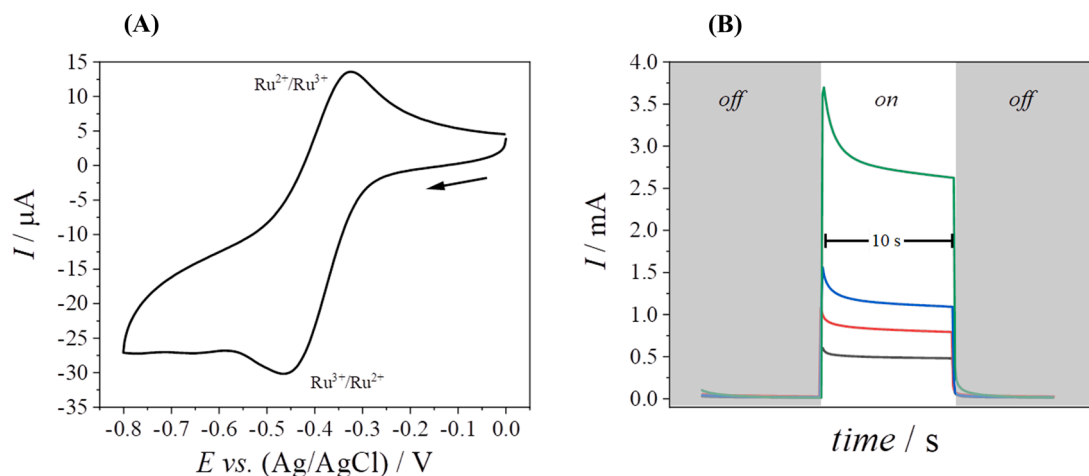
Fig. 5. (A) cyclic voltammogram obtained for SPE/c-g-C$_3$N$_4$ in 0.1 mol L^{-1} phosphate buffer saline, pH 7.0, containing 1 mmol L-1 [Ru(NH3)6]Cl3; scan rate of 0.05 V s-1 and step potential of 0.002 V. (B) photocurrents recorded for SPE/c-g-C$_3$N$_4$ in 0.1 mol L^{-1} phosphate buffer saline.
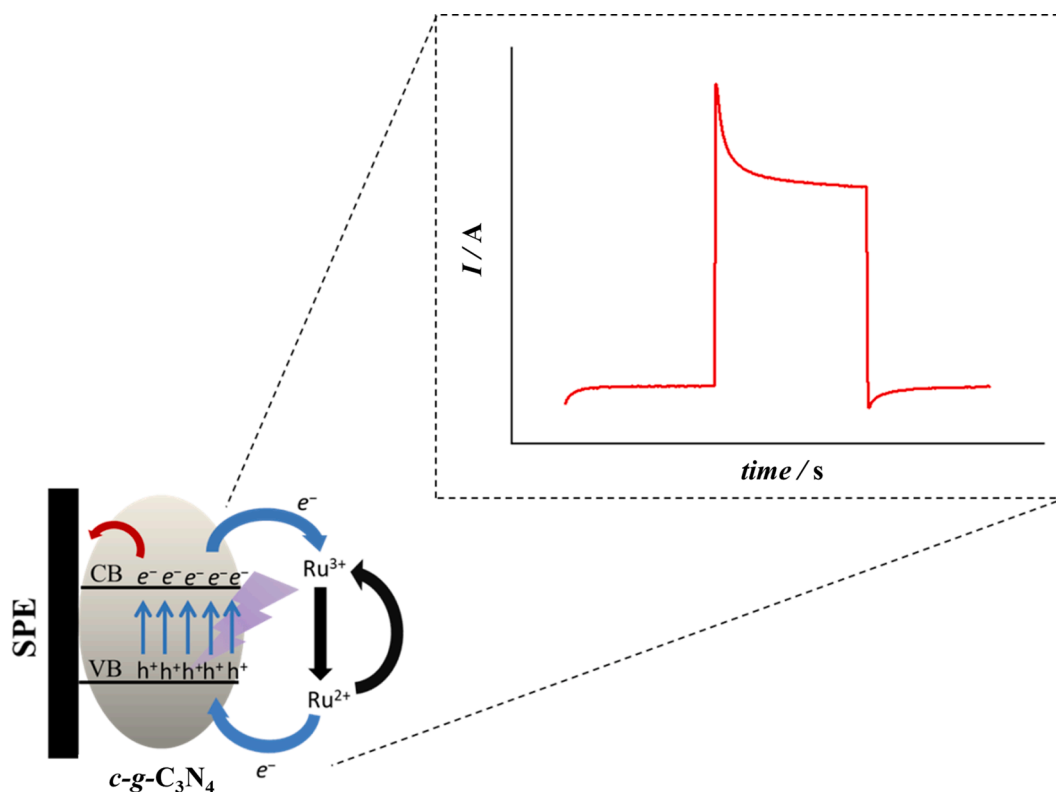
Fig. 6. A mechanism for photocurrent generation in a printed carbon electrode coated with carbonylated graphitic carbon nitride (c-g-C$_3$N$_4$) in the presence of 0.1 mol L^{-1} phosphate buffer saline at pH 7.0 containing [Ru(NH3)6]Cl3 at 0 V.

verified in an experiment shown in Fig. 5B. As can be seen, as the concentration of [Ru(NH$_3$)$_6$]Cl$_3$ increased, an increase in the generated photocurrent was observed due to the charge transferred from the complex to the semiconductor. In this experiment, the UV light was irradiated intermittently on the surface of the device in on/off intervals of 10 s.

The mechanism for photocurrent generation is illustrated in Fig. 6.

When the device is irradiated by UV light, charge separation in the *c-g-*C$_3$N$_4$ band structure (*n*-type semiconductor) occurs, with the promotion of electrons (*e*$^-$) of the valence band for the conduction band. Thereby, the presence of vacancies (*h*$^+$) in the valence band predominates. The recombination between the promoted electrons and vacancies occurs in the absence of a charge-accepting species in contact with the semiconductor, which reduces the intensity of the generated photocurrent.
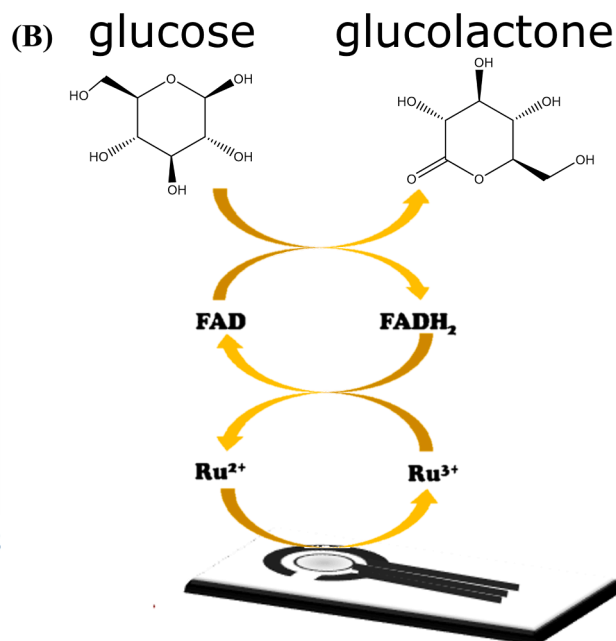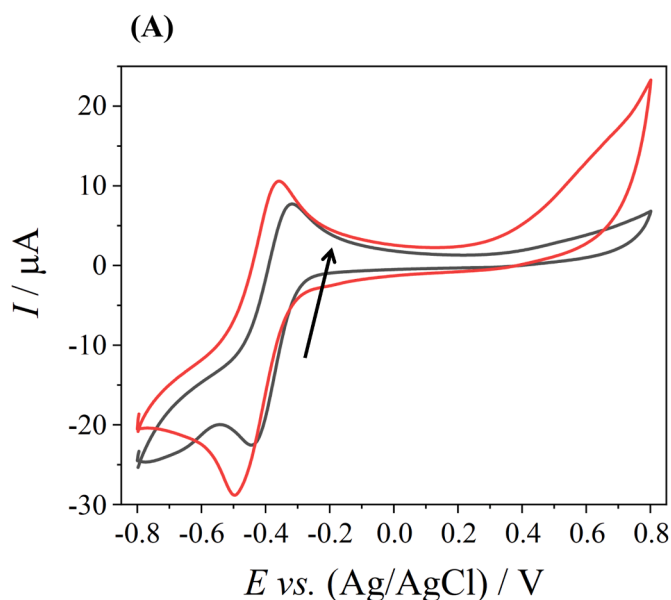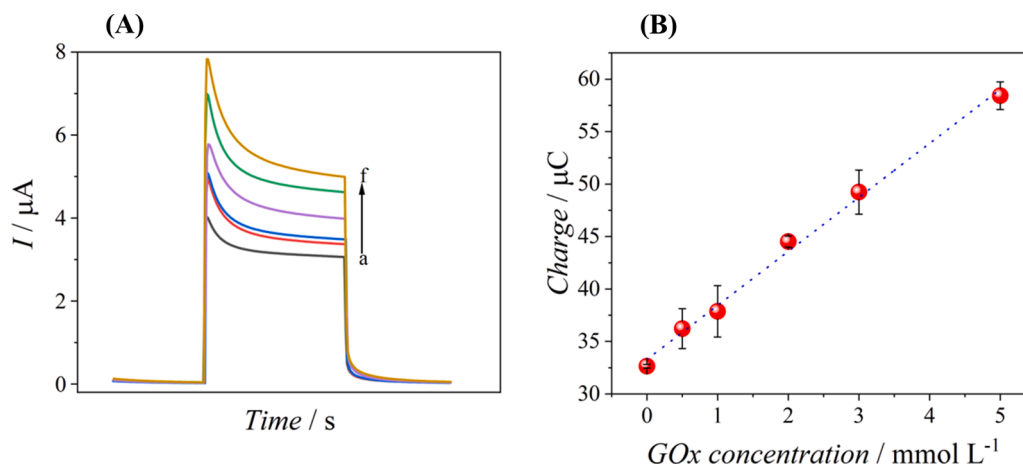

Fig. 7. (A) cyclic voltammograms for SPE/c-g-C$_3$N$_4$/GOx in the absence of glucose (black line) and the presence of 5 mmol L^{-1} glucose (red line); using 0.1 mol L^{-1} phosphate buffer saline (pH 7.0) as supporting electrolyte; scan rate of 0.05 V s^{-1}. (B) Proposed mechanism.

(A)

(B)

Fig. 8. A) Photocurrents for concentrations of (a) 0; (b) 0.5; (c) 1; (d) 2; (e) 3 and (f) 5 mmol L−1, at 0 V, in 0.1 mol L^{-1} phosphate buffer saline (pH 7.0). (B) Linear regression of charge transfer versus concentration for biocatalytic glucose oxidation.

When the $[Ru(NH_3)_6]Cl_3$ is present, it acts as an acceptor of some of the electrons promoted to the conduction band. During this process, Ru^{3+} is reduced to Ru^{2+}. The reduced form of ruthenium acts as an acceptor of valence band vacancies releasing an electron that causes the oxidized form regeneration. These processes with ruthenium complex are responsible for preventing the recombination of charges inside the semiconductor. Thus, the rate of electrons transferred from the conduction band to the transducer increases and provides the highest intensity of the generated photocurrent.

3.5. Analytical performance of the photoelectrochemical device for glucose quantification

Experiments were carried out using c-g-C_3N_4 for photoelectrochemical sensing of glucose. This approach is devoted as proof of concept to evaluate the carbonylic group capability for binding with terminal groups from biomolecules, in this case, the GOx enzyme. Previously, the catalytic activity of the GOx was verified through cyclic voltammetry in the absence and presence of glucose. The cyclic voltammogram of Fig. 7A shows a typical behavior of second-generation biosensors [41] for the device with GOx immobilized over c-g-C_3N_4. Furthermore, Fig. 7B has proposed the mechanism of the biosensor for the biocatalytic oxidation of glucose to glucolactone. In the first step, the flavin adenine dinucleotide (FAD) from the active center of GOx acts as an electron mediator for glucose oxidation, whereas it is reduced to flavin adenine dinucleotide ($FADH_2$). Next, in the second step, $FADH_2$ is converted to FAD and the electron involved in this process is transferred to Ru^{3+} of $[Ru(NH_3)_6]Cl_3$ which reduces to Ru^{2+}. The electron transfer from the Ru^{2+} to the transducer causes de conversion to Ru^{3+}.

Under UV irradiation, the device generates photocurrents at controlled potential, and the intensity increases proportionally to the increase of glucose amount present in the sample. The supplementary material shows the results of the dependence of the charge transferred during the biocatalytic glucose oxidation with GOx units immobilized per electrode (Fig. 2S) and the applied potential (Fig. 3S). For the calculation of the transferred charge, the photocurrent signal was integrated.

The signal intensity varied no more than 5% with the increase of the applied potential value. Then, 0 V was chosen due to the low interference of possible electroactive species present in a real sample (*e.g.* blood, saliva, or urine). Furthermore, the application of the SPE/c-g-C_3N_4/GOx with GOx 20 U per electrode presented the best performance. Therefore, the above conditions were adopted for further experiments. The analytical performance of the photoelectrochemical sensor was evaluated for glucose concentrations from 0 mol L^{-1} to 5.00 mmol L^{-1} ($n = 4$)

Table 1

Data from photoelectrochemical devices are found in the literature for glucose determination.

Device	Applied potential / V	Linear range / mol L^{-1}	L.O.D. / mol L^{-1}	Refs.
FTO/BiVO$_4$	+0.15*	$0 - 5.0\times10^{-3}$	1.3×10^{-7}	[43]
Ti/ATO	+0.5**	$3.8\times10^{-4} - 6.7\times10^{-4}$	7.8×10^{-6}	[44]
FTO/ZnO-Au-Cu2O/GOx	0.0*	$1.0\times10^{-3} - 1.9\times10^{-4}$	8.0×10^{-5}	[45]
ITO/g-CN/α-Fe$_2$O$_3$	+0.3*	$5.6\times10^{-7} - 6.4\times10^{-5}$	1.7×10^{-7}	[46]
Au/Cu/ZnSe QDs	-0.3*	$0 - 6.0\times10^{-3}$	-	[47]
SPE/c-g-C$_3$N$_4$/GOx	0.0*	$0 - 5.0\times10^{-3}$	4.3×10^{-4}	**This work**

* versus Ag/AgCl.
** versus SCE.

in 0.1 mol L^{-1} phosphate buffer saline (pH 7.0). Fig. 8A shows a typical increase of generated photocurrent with the increase of the glucose in the sample, which corroborates the proposed mechanism for the biocatalysis of glucose. The analytical curve (*Charge*/μC = 33.3 mmol L^{-1}/μC ($\pm$ 0.45) + 5.15 ($\pm$ 0.19) ×*GOx*/mmol L^{-1}; $R^2 = 0.995$) was obtained for the linear correlation of transferred charge during the biocatalysis, through integration of photocurrent signal. The limit of detection (L.O.D.) was calculated according to Miller-Miller [42], yielding 0.43 mmol L^{-1}, while repeatability intra-day ($n = 10$) and inter-day ($n = 10$) yielded values of 1.1% and 1.8%, respectively.

Table 1 summarizes the data of photoelectrochemical devices for glucose determination found in the literature. The device designed here presented an acceptable performance at 0 V, which is advantageous, since in the applied potential the interference of foreign species is avoided. Moreover, the miniaturized layout requires a low sample

Table 2

Data of glucose determination in a real sample (urine).

*Sample	Theoretical concentration / mol L^{-1}	Real concentration / mol L^{-1}	Recovery / %	RSD / %
1	Unknown	8.00×10^{-4}	Not applicable	5.3
2	1.50×10^{-3}	1.44×10^{-3}	96.0	5.4
3	2.50×10^{-3}	2.42×10^{-3}	96.8	5.0
4	5.00×10^{-3}	4.88×10^{-3}	97.6	4.7

*($n = 3$)

volume (200 μL) and allows the portability for future applications as a point of care test. No inference was made over the LOD values, considering that different calculation methods were adopted in each reference.

Analytical performance was also tested for glucose determination in a urine sample. Table 2 shows the data for the concentration of glucose present in sample 1 calculated through the standard addition method. Furthermore, known concentrations of spiked samples (2, 3, and 4) were tested for recovery percentage. All results are satisfactory and suggest that the use of the device, in an easy and non-invasive way, is promising, since the typical concentration of glucose in the urine is of the order of mmol L^{-1}

Sensor selectivity was tested in the presence of possible interferents found in urine. Thus, a 0.1 mol L^{-1} phosphate buffer saline was prepared with 5 mmol L^{-1} glucose and the following species present: NH_4^+, Ca^{2+}, Mg^+, Cl^-, creatine, urea, uric acid, phosphorus, oxalic acid, and citric acid. No interference was observed in the sensor response, which indicates its robustness and potential for glucose determination in urine samples.

4. Conclusion

The organic semiconductor 2D-carbonylated graphitic carbon nitride (c-g-C_3N_4), was successfully synthesized from melamine, using thermal treatment followed by acid and sonochemical steps. Morphological and structural characterizations proved the occurrence of sheets composed of nanometer particles functionalized majority with a carbonyl group. These features are desirable for the material application in photoelectrochemical sensors modified with biological molecules. To illustrate the potential application, a carbon SPE was modified with c-g-C_3N_4 and then GOx was immobilized on the material. The device was applied for glucose monitoring in urine samples yielding a suitable limit of detection and no effect of interferents. Our results indicate the potential of the miniaturized, disposable, low-cost, and low sample volume photoelectrochemical device for monitoring molecules of medical and biological.

CRediT authorship contribution statement

Thiago Martimiano do Prado: Conceptualization, Methodology, Writing – review & editing, Data curation, Writing – original draft. **Lucas Gomes da Silva Catunda:** Visualization, Investigation, Data curation. **Marcelo Luiz Calegaro:** Visualization, Investigation, Data curation. **Daniel Souza Correa:** Supervision, Writing – original draft. **Sérgio Antonio Spinola Machado:** Supervision, Validation.

Declaration of Competing Interest

The authors declare that they have no known competing financial interests or personal relationships that could have appeared to influence the work reported in this paper.

Acknowledgments

Supplementary materials

Supplementary material associated with this article can be found, in the online version, at doi:10.1016/j.electacta.2022.141094.

References

[1] S. Yang, R.L. Zhou, Y.J. Huang, Surface plasmon resonance and field confinement in graphene nanoribbons in a nanocavity, Front. Phys. 16 (2021), https://doi.org/10.1007/s11467-021-1060-2.

[2] D. Zhao, W. Chang, C. Lu, C. Yang, K. Jiang, X. Chang, H. Lin, F. Zhang, S. Han, Z. Hou, X. Zhuang, Charge transfer salt and graphene heterostructure-based micro-supercapacitors with alternating current line-filtering performance, Small 15 (2019) 1–9, https://doi.org/10.1002/smll.201901494.

[3] C. Xue, H. Gao, G. Hu, Viscoelastic and fatigue properties of graphene and carbon black hybrid structure filled natural rubber composites under alternating loading, Constr. Build. Mater. 265 (2020), 120299, https://doi.org/10.1016/j.conbuildmat.2020.120299.

[4] S.A. Csiszar, D.E. Meyer, K.L. Dionisio, P. Egeghy, K.K. Isaacs, P.S. Price, K. A. Scanlon, Y.M. Tan, K. Thomas, D. Vallero, J.C. Bare, Conceptual framework to extend life cycle assessment using near-field human exposure modeling and high-throughput tools for chemicals, Environ. Sci. Technol. 50 (2016) 11922–11934, https://doi.org/10.1021/acs.est.6b02277.

[5] J.M. Gernand, Particulate matter: fine and ultrafine — how emerging data on engineered nanomaterials may change how we regulate worker exposures to dust 14 (2015), https://doi.org/10.1115/IMECE2015-53056.

[6] T.O. Monteiro, C.C. dos Santos, T.M. do Prado, F.S. Damos, R.C.S. Luz, O. Fatibello-Filho, Highly sensitive photoelectrochemical immunosensor based on anatase/rutile TiO_2 and Bi_2S_3 for the zero-biased detection of PSA, J. Solid State Electrochem. 24 (2020), https://doi.org/10.1007/s10008-020-04637-8.

[7] H. Li, Y. Zhao, M. Yue, G. Jie, Signal-off photoelectrochemical biosensing platform based on hybridization chain-doped manganese porphyrin quenching on CdSe signal coupling with cyclic amplification for thrombin detection, J. Electroanal. Chem. 879 (2020), https://doi.org/10.1016/j.jelechem.2020.114803.

[8] Y. Qin, J. Wen, L. Zheng, H. Yan, L. Jiao, X. Wang, X. Cai, Y. Wu, G. Chen, L. Chen, L. Hu, W. Gu, C. Zhu, Single-atom-based heterojunction coupling with ion-exchange reaction for sensitive photoelectrochemical immunoassay, Nano Lett. 21 (2021) 1879–1887, https://doi.org/10.1021/acs.nanolett.1c00076.

[9] Y. Xing, X. Chen, B. Jin, P. Chen, C. Huang, Z. Jin, Photoelectrochemical aptasensors constructed with photosensitive PbS quantum Dots/TiO_2 nanoparticles for detection of kanamycin, Langmuir 37 (2021) 3612–3619, https://doi.org/10.1021/acs.langmuir.0c03593.

[10] A. Nasri, M. Petrissans, V. Fierro, A. Celzard, Gas sensing based on organic composite materials: review of sensor types, progresses and challenges, Mater. Sci. Semicond. Process. 128 (2021), https://doi.org/10.1016/j.mssp.2021.105744.

[11] M. Can, S. Demirci, A.K. Sunol, N. Sahiner, An amino acid, L-Glutamic acid-based metal-organic frameworks and their antibacterial, blood compatibility, biocompatibility, and sensor properties, Microporous Mesoporous Mater. 309 (2020), https://doi.org/10.1016/j.micromeso.2020.110533.

[12] A. Abun, B.R. Huang, A. Saravanan, D. Kathiravan, P.D. Hong, Exfoliated $MoSe_2$ nanosheets doped on the surface of ZnO nanorods for hydrogen sensing applications, ACS Appl. Nano Mater. 3 (2020) 12139–12147, https://doi.org/10.1021/acsanm.0c02641.

[13] L.A. Mercante, V.P. Scagion, F.L. Migliorini, L.H.C. Mattoso, D.S. Correa, Electrospinning-based (bio)sensors for food and agricultural applications: a review, TrAC Trends Anal. Chem. 91 (2017) 91–103, https://doi.org/10.1016/J.TRAC.2017.04.004.

[14] J. Shu, D. Tang, Recent advances in photoelectrochemical sensing: from engineered photoactive materials to sensing devices and detection modes, Anal. Chem. 92 (2020) 363–377, https://doi.org/10.1021/acs.analchem.9b04199.

[15] R. Wang, K. Yan, F. Wang, J. Zhang, A highly sensitive photoelectrochemical sensor for 4-aminophenol based on CdS-graphene nanocomposites and molecularly imprinted polypyrrole, Electrochim. Acta 121 (2014) 102–108, https://doi.org/10.1016/j.electacta.2013.12.139.

[16] Y. Zhou, H. Yin, S. Ai, Applications of two-dimensional layered nanomaterials in photoelectrochemical sensors: a comprehensive review, Coord. Chem. Rev. 447 (2021), https://doi.org/10.1016/j.ccr.2021.214156.

[17] J. Wang, Z. Liu, Recent advances in two-dimensional layered materials for photoelectrochemical sensing, TrAC Trends Anal. Chem. 133 (2020), https://doi.org/10.1016/j.trac.2020.116089.

[18] M. Li, G. Zhang, C. Feng, H. Wu, H. Mei, Highly sensitive detection of chromium (VI) by photoelectrochemical sensor under visible light based on Bi SPR-promoted $BiPO_4$/BiOI heterojunction, Sens. Actuators B 305 (2020), 127449, https://doi.org/10.1016/j.snb.2019.127449.

[19] B. Luo, Y. Zhao, D. Jing, State-of-the-art progress in overall water splitting of carbon nitride based photocatalysts, Front. Energy (2021), https://doi.org/10.1007/s11708-021-0737-0.

[20] C. Hu, F. Chen, Y. Wang, N. Tian, T. Ma, Y. Zhang, H. Huang, Exceptional cocatalyst-free photo-enhanced piezocatalytic hydrogen evolution of carbon nitride nanosheets from strong in-plane polarization, Adv. Mater. (2021), https://doi.org/10.1002/adma.202101751.

[21] X. Zou, Z. Sun, Y.H. Hu, g-C_3N_4-based photoelectrodes for photoelectrochemical water splitting: a review, J. Mater. Chem. A 8 (2020) 21474–21502, https://doi.org/10.1039/d0ta07345h.

[22] L. Mao, X. Xue, X. Xu, W. Wen, M.M. Chen, X. Zhang, S. Wang, Heterostructured CuO-g-C_3N_4 nanocomposites as a highly efficient photocathode for photoelectrochemical aflatoxin B1 sensing, Sens. Actuators B 329 (2021), 129146, https://doi.org/10.1016/J.SNB.2020.129146.

[23] C. Yuan, Z. He, Q. Chen, X. Wang, C. Zhai, M. Zhu, Selective and efficacious photoelectrochemical detection of ciprofloxacin based on the self-assembly of 2D/2D g-C_3N_4/Ti_3C_2 composites, Appl. Surf. Sci. 539 (2021), 148241, https://doi.org/10.1016/J.APSUSC.2020.148241.

[24] Z. Zhang, B. Peng, X. Ouyang, X. Zhu, L. Chen, X. Fan, Z. Zhou, J. Wang, L. Tang, A self-powered photoelectrochemical aptasensor based on dual-photoelectrode photofuel cell for chloramphenicol detection, Sens. Actuators B 368 (2022), 132144, https://doi.org/10.1016/J.SNB.2022.132144.

[25] J. Li, C. Wang, X. Chen, M. Huang, Q. Fu, R. Li, Y. Wang, C. Li, P. Zhao, Y. Xie, J. Fei, A non-enzymatic photoelectrochemical sensor based on g-C$_3$N$_4$@CNT heterojunction for sensitive detection of antioxidant gallic acid in food, Food Chem. 389 (2022), 133086, https://doi.org/10.1016/J.FOODCHEM.2022.133086.

[26] S.S. Low, Z. Chen, Y. Li, Y. Lu, Q. Liu, Design principle in biosensing: critical analysis based on graphitic carbon nitride (G-C$_3$N$_4$) photoelectrochemical biosensor, TrAC Trends Anal. Chem. 145 (2021), 116454, https://doi.org/10.1016/J.TRAC.2021.116454.

[27] S. Velmurugan, T.C.K. Yang, Fabrication of high-performance molybdenum disulfide-graphitic carbon nitride p-n heterojunction stabilized rGO/ITO photoelectrode for photoelectrochemical determination of dopamine, ACS Appl. Electron. Mater. 2 (2020) 2845–2856, https://doi.org/10.1021/acsaelm.0c00500.

[28] Y. Wang, Y. Cheng, N. Wu, Z. Zhang, Graphitic carbon nitride/poly(3-hexylthiophene) nanocomposites for the photoelectrochemical detection of H$_2$O$_2$ in living cells, ACS Appl. Nano Mater. 3 (2020) 8598–8603, https://doi.org/10.1021/acsanm.0c02114.

[29] L. Xu, W. Duan, F. Chen, J. Zhang, H. Li, A photoelectrochemical aptasensor for the determination of bisphenol A based on the Cu (I) modified graphitic carbon nitride, J. Hazard. Mater. 400 (2020), https://doi.org/10.1016/j.jhazmat.2020.123162.

[30] Y. Chen, L. Xu, J. Dong, P. Yan, F. Chen, J. Qian, H. Li, An enhanced photoelectrochemical ofloxacin aptasensor using NiFe layered double hydroxide/graphitic carbon nitride heterojunction, Electrochim. Acta 368 (2021), https://doi.org/10.1016/j.electacta.2020.137595.

[31] J. Wang, Z. Liu, Recent advances in two-dimensional layered materials for photoelectrochemical sensing, TRAC Trends Anal. Chem. 133 (2020), https://doi.org/10.1016/j.trac.2020.116089.

[32] X. Hu, Y. Hu, Q. Zhang, Y. Yu, Y. Wang, Efficient synthesis of porous graphitic carbon nitride nano - sheets with different precursors via thermal condensation, Mater. Test. 62 (2020) 378–382, https://doi.org/10.3139/120.111493.

[33] S. Yang, Y. Gong, J. Zhang, L. Zhan, L. Ma, Z. Fang, R. Vajtai, X. Wang, P. M. Ajayan, Exfoliated graphitic carbon nitride nanosheets as efficient catalysts for hydrogen evolution under visible light, Adv. Mater. 25 (2013) 2452–2456, https://doi.org/10.1002/adma.201204453.

[34] N. Briggs, S. Subramanian, Z. Lin, X. Li, X. Zhang, K. Zhang, K. Xiao, D. Geohegan, R. Wallace, L.Q. Chen, M. Terrones, A. Ebrahimi, S. Das, J. Redwing, C. Hinkle, K. Momeni, A. van Duin, V. Crespi, S. Kar, J.A. Robinson, A roadmap for electronic grade 2D materials, 2D Mater. 6 (2019), 022001, https://doi.org/10.1088/2053-1583/AAF836.

[35] T.M. do Prado, C.C. Badaró, R.G. Machado, P.S. Fadini, O. Fatibello-Filho, F. C. Moraes, Using bismuth vanadate/copper oxide nanocomposite as photoelectrochemical sensor for naproxen determination in sewage, Electroanalysis 32 (2020) 1930–1937, https://doi.org/10.1002/ELAN.202000055.

[36] F. Cheng, H. Wang, X. Dong, The amphoteric properties of g-C$_3$N$_4$ nanosheets and fabrication of their relevant heterostructure photocatalysts by an electrostatic re-assembly route, Chem. Commun. 51 (2015) 7176–7179, https://doi.org/10.1039/c5cc01035g.

[37] P.A. Raymundo-Pereira, N.O. Gomes, S.A.S. Machado, O.N. Oliveira, Simultaneous, ultrasensitive detection of hydroquinone, paracetamol and estradiol for quality control of tap water with a simple electrochemical method, J. Electroanal. Chem. 848 (2019), https://doi.org/10.1016/j.jelechem.2019.113319.

[38] F. Fina, S.K. Callear, G.M. Carins, J.T.S. Irvine, Structural investigation of graphitic carbon nitride via XRD and neutron diffraction, Chem. Mater. 27 (2015) 2612–2618, https://doi.org/10.1021/ACS.CHEMMATER.5B00411.

[39] J. Zhou, Y. Tada, Y. Kato, Y. Nagatsu, R. Takebayashi, K. Iwata, K. Yasui, Y. Sakaguchi, Effect of mixing on sonochemical reaction in a sonoreactor, J. Chem. Eng. Jpn. 43 (2010) 657–660, https://doi.org/10.1252/JCEJ.09WE235.

[40] D. Ayodhya, G. Veerabhadram, Influence of g-C$_3$N$_4$ and g-C$_3$N$_4$ nanosheets supported CuS coupled system with effect of pH on the catalytic activity of 4-NP reduction using NaBH4, Flatchem 14 (2019), https://doi.org/10.1016/j.flatc.2019.100088.

[41] D.P. Dutta, D. Dagar, Efficient selective sorption of cationic organic pollutant from water and its photocatalytic degradation by AlVO$_4$/g-C$_3$N$_4$ nanocomposite, J. Nanosci. Nanotechnol. 20 (2020) 2179–2194, https://doi.org/10.1166/jnn.2020.17333.

[42] A. Navarro-Aguilar I, S. Obregon, D. Sanchez-Martinez, D.B. Hernandez-Uresti, An efficient and stable WO$_3$/g-C$_3$N$_4$ photocatalyst for ciprofloxacin and orange G degradation, J. Photochem. Photobiol. A Chem. 384 (2019), https://doi.org/10.1016/j.jphotochem.2019.112010.

[43] B. Wang, X. Li, H. Wu, G. Xu, X. Zhang, X. Shu, J. Lv, Y. Wu, Synthesis of Ni-MoSx/g-C$_3$N$_4$ for photocatalytic hydrogen evolution under visible light, ChemCatChem 12 (2020) 911–916, https://doi.org/10.1002/cctc.201901654.

[44] D.B. Hernandez-Uresti, D. Sanchez-Martinez, L.M. Torres-Martinez, Novel visible light-driven PbMoO$_4$/g-C$_3$N$_4$ hybrid composite with enhanced photocatalytic performance, J. Photochem. Photobiol. A Chem. 345 (2017) 21–26, https://doi.org/10.1016/j.jphotochem.2017.05.013.

[45] J. Kröger, A. Jiménez-Solano, G. Savasci, V.W. h. Lau, V. Duppel, I. Moudrakovski, K. Küster, T. Scholz, A. Gouder, M.L. Schreiber, F. Podjaski, C. Ochsenfeld, B. V. Lotsch, Morphology control in 2D carbon nitrides: impact of particle size on optoelectronic properties and photocatalysis, Adv. Funct. Mater. (2021), 2102468, https://doi.org/10.1002/adfm.202102468.

[46] P.R. Davies, D.J. Morgan, Practical guide for X-ray photoelectron spectroscopy: applications to the study of catalysts, J. Vac. Sci. Technol. A Vac. Surf. Films 38 (2020), 033204, https://doi.org/10.1116/1.5140747.

[47] J. Kröger, A. Jiménez-Solano, G. Savasci, V.W. h. Lau, V. Duppel, I. Moudrakovski, K. Küster, T. Scholz, A. Gouder, M.-L. Schreiber, F. Podjaski, C. Ochsenfeld, B. V. Lotsch, Morphology control in 2D carbon nitrides: impact of particle size on optoelectronic properties and photocatalysis, Adv. Funct. Mater. 31 (2021), 2102468, https://doi.org/10.1002/ADFM.202102468.

[48] L. Zhang, G. Ye, X. Huo, S. Xu, S. Chen, K. Matyjaszewski, Structural engineering of graphitic carbon nitrides for enhanced metal-free PET-RAFT polymerizations in heterogeneous and homogeneous systems, ACS Omega 4 (2019) 16247–16255, https://doi.org/10.1021/ACSOMEGA.9B02597.

[49] A. Akhundi, E.I. García-López, G. Marcì, A. Habibi-Yangjeh, L. Palmisano, Comparison between preparative methodologies of nanostructured carbon nitride and their use as selective photocatalysts in water suspension, Res. Chem. Intermed. 43 (9. 43) (2017) 5153–5168, https://doi.org/10.1007/S11164-017-3046-9, 2017.